7
Zinc Titanate as a Photoelectrode Material for Quantum Dot Sensitized Solar Cells

7.1 Introduction

In Quantum Dot Sensitized Solar Cells, efforts towards improving efficiency include manipulation of QDs absorber along with development of photoelectrode material. Nanostructured photoelectrode plays key role in transportation of injected photoexcited carriers. Apart from widely used nanostructured binary oxide such as ZnO and TiO_2 [Jose et al., 2009], the requirement to achieve higher electron mobility in photoelectrode material and desire to reduce oxidative holes in valence band have pushed researchers towards exploring alternative to these widely used photoelectrode material. In past others photoelectrode materials have been explored as photoelectrode material in QDSSCs like SnO_2 [Hossain et al., 2011], Nb_2O_5 [Viet et al., 2010], Zn_2SnO_4 [Choi et al., 2013], $BaTiO_3$ [Meng et al., 2014], $SrTiO_3$ [Burnside et al., 1999] and $ZnTiO_3$ [Habibi et al., 2012]. However, power conversion efficiency is reported low with these photoelectrode materials as compared to TiO_2.

Zinc and titanium based ternary oxide nanomaterial are important as a photoelectrode material for QDSSCs with expectation of better corrosion resistance and better electrical and optical properties. Better electrical properties can enhance carrier lifetime in photoelectrode material resulting in improvement in power conversion efficiency [Hod and Zaban, 2014]. So these ternary oxides have potential to show better electron lifetime and lower carrier recombination [J. Yu et al., 2016]. Relative bandgap positions of these wide bandgap semiconductor materials are very important in QDSSCs. Relative position of conduction band minima (CBM) with conduction energy level of QDs is very important for efficient electron acceptance while band alignment with selective contact is also important for efficient carrier collection at contact. Carrier mobility is another important parameter of these wide bandgap semiconductor materials that can lead to lower recombination probabilities of injected electrons. Zinc titanate also has been explored as a photoelectrode material. In some of the reports, zinc titanate is reported to have higher electron mobility than TiO_2 showing potential for better photovoltaic response in QDSSCs [J. Yu et al., 2016]. In some reports, zinc titanate is reported to outperform TiO_2 [Burnside et al., 1999].

Zinc titanate is reported to exist in Zn_2TiO_4, $ZnTiO_3$, $Zn_2Ti_3O_8$ [Denosb, 1996] and cubic $ZnTiO_3$, however structural stability of cubic zinc titanate is not well understood [C. Li et al., 2000]. Zinc titanate is considered as highly doped anatase TiO_2 due to its structural similarity [Conesa, 2013]. Zinc titanate exhibits six fold octahedral coordination, similar to titanium arrangement in anatase TiO_2. Zinc titanate exists in three crystallographic phases namely zinc meta titanate ($ZnTiO_3$) in rhombohedral ilmenite structure, zinc orthotitanate (Zn_2TiO_4) in cubic spinal structure and $Zn_2Ti_3O_8$ in cubic defect spinel structure [Denosb, 1996]. $Zn_2Ti_3O_8$ has been reported as metastable form of zinc titanate and it decomposes in Zn_2TiO_4 and TiO_2 at temperature more than 945 °C [Denosb, 1996]. Few reports also predict cubic $ZnTiO_3$ but detailed crystallographic information is not available.

7.2 Experimental Procedure

In this work, zinc titanate nanoparticles are synthesized using sol-gel process as described in section 4.1.2.1 and calcinated at various temperatures and duration to investigate transformation of different crystallographic phase of zinc titanate. Prepared zinc titanate nanoparticle powder is used to prepare paste for Dr. blade and photoelectrodes for QDSSC are prepared using Dr. blade method as described in sections 4.1.2.2 and 4.1.2.3, respectively. Prepared electrodes are sensitized with cadmium sulfide (CdS) using SILAR process as discussed in section 4.1.3.1. ZnS surface passivation is also performed on CdS QDs sensitized electrode as described in section 4.1.3.3. Cu_2S counter electrode is prepared as described in section 4.1.5.2 and polysulfide electrolyte is prepared as described in section 4.1.4. Photovoltaic response of prepared QDSSC is investigated using Cu_2S as counter electrode and polysulfide electrolyte as red-ox electrolyte as described in section 4.2.3.1. The effect of phase composition and surface morphology of zinc titanate are discussed for photovoltaic performance of prepared QDSSCs. The lower calcinated zinc titanate nano-powder performed better as compared to higher temperature calcinated zinc titanate nano-powder.

Structural characterization of zinc titanate nano powder and sensitized electrode was done using XRD as described in section 4.2.1.1. Scanning electron microscopy was utilized in SE mode to image surface morphology of sintered electrode as described in section 4.2.1.2. Optical properties of prepared zinc titanate nano powder were calculated using diffuse reflectance accessory with Cary 4000 as described in section 4.2.2.1. Vibrational spectra of calcinated powder were recorded using FTIR as described in section 4.2.2.2. QDSSC is assembled with sensitized zinc titanate photoelectrode for photovoltaic and impedance characterizations, as described in sections 4.2.3.1 and 4.2.3.2, respectively.

7.3 Results and Discussion

7.3.1 X-ray Diffraction Analysis

As discussed in section 4.1.2.1 that zinc titanate nano powder is calcinated at different temperature and duration. X-ray diffraction pattern is collected for all these samples and shown in Figure 7.1 with appropriate label. Peak positions of cubic zinc $Zn_2Ti_3O_8$ (ICDD 01-087-1781), cubic Zn_2TiO_4 (ICDD 00-025-1164) and hexagonal $ZnTiO_3$ (ICDD 00-026-1500) are marked in X-ray diffraction pattern with square symbol using different colors. X-ray diffraction pattern analysis suggests that prepared zinc titanate nano powder samples are not phase pure and have different crystallographic phases. Even though, lower 2 θ peaks at 23° and 25° are reported to be characteristics peaks of cubic $ZnTiO_3$ but a close observation reveals the peak doublets at higher 2 θ angle, indicating presence of cubic Zn_2TiO_4 in prepared nano powder. In solid state reactions, presence of Zn_2TiO_4 phase at lower temperature depends on starting material composition [Denosb, 1996]. This study signifies presence of Zn_2TiO_4 at lower calcination temperature with $Zn_2Ti_3O_8$ phase. At higher calcination temperature, $Zn_2Ti_3O_8$ starts converting into Zn_2TiO_4 and hexagonal $ZnTiO_3$ and $Zn_2Ti_3O_8$ phase disappear completely.

Reference Intensity Ratio (RIR) method was adopted to estimate qualitative phase fraction of different phases of zinc titanate [Hubbard and Snyder, 1988]. The relative intensities of XRD diffraction peaks were analyzed. Intensity of a diffraction peak depends upon relative phase fraction in a mixed phase sample as

$$I_a = \frac{K_a X_a}{\rho_a \mu}$$

where I_a is XRD intensity of a certain phase, K_a is the structure factor, X_a is respective weight fraction of phase, ρ_a is the density of the respective phase and μ is linear attenuation coefficient. Reference intensity for I/I_{cor} was taken for different crystallographic phases from respective ICDD database files. Figure 7.2 (a) shows phase fraction of different crystallographic phases in

calcinated zinc titanate nano powder calculated using RIR method against calcination temperatures.

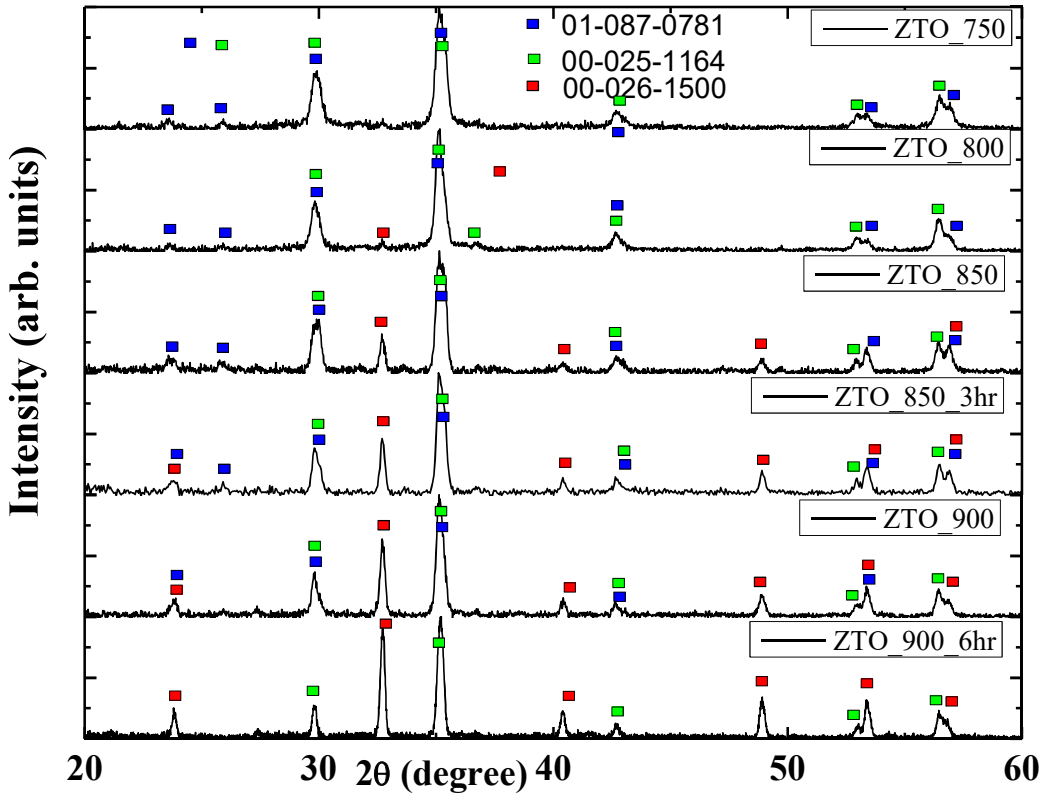

Figure: 7.1 X-ray diffraction pattern for zinc titanate nano powder for different calcination temperature and duration as indicated by labels.

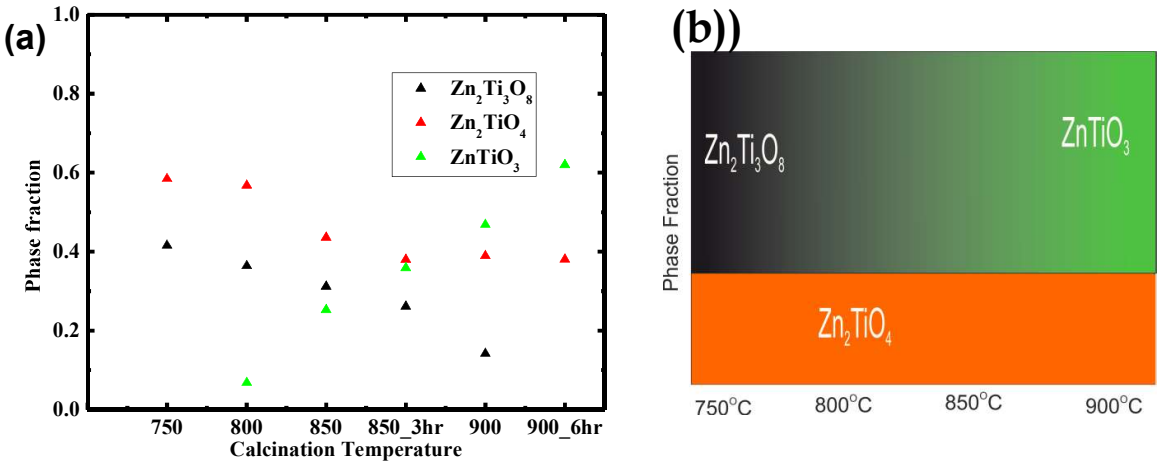

Figure: 7.2 (a) Estimated phase fraction of zinc titanate crystallographic phases and (b) schematic diagram for phase fraction variation with calcination temperature.

Zn_2TiO_4 and $Zn_2Ti_3O_8$ diffraction peaks are closely spaced and are deconvoluted using FITYK software [Abràmoff et al., 2004]. Deconvoluted peaks with < 5% error in respective relative reference intensity are only considered for phase fraction calculation. The schematic representation of evolution of crystallographic phases against calcination temperature is summarized in Figure 7.2 (b).

$Zn_2Ti_3O_8$ start converting into hexagonal $ZnTiO_3$ at higher calcination temperature, as can be seen from crystallographic phase diagram, Figure 7.2 (b). At 900 °C, for 6 hour calcination duration $Zn_2Ti_3O_8$ converts completely into hexagonal $ZnTiO_3$, Figure 7.2 (b). Zn_2TiO_4 is considered as the most stable phase of zinc titanate and phase fraction analysis suggests that Zn_2TiO_4 phase is higher for lower calcination temperature while nearly constant for higher calcination temperatures. In solid state reaction, with equal molar ratio of zinc and titanium precursors, Zn_2TiO_4 phase exists at higher fraction but at higher calcination temperature, phase fraction shows strong dependence on calcination temperature. Phase diagram was reported in 1996 for solid state reaction with calcination temperature, confirming that $Zn_2Ti_3O_8$ is a low temperature form of hexagonal $ZnTiO_3$ and at higher calcination temperature it converts into cubic Zn_2TiO_4 and rutile TiO_2. However, at lower calcination temperatures, phase composition is not so clear [Denosb, 1996]. Few reports also state the existence of cubic $ZnTiO_3$ matched with ICDD database file 00-039-0190 which was originally reported as low temperature form of $Zn_2Ti_3O_8$ and ICDD database file does not contain detailed crystallographic information, thus, a clear understanding is still missing for zinc titanate system [Yamaguchi et al., 1987].

7.3.2 Investigation of Electronic Properties of Zinc Titanate Nano Powder

To identify electronic transitions of different crystallographic phases of zinc titanate, diffuse reflectance measurements were carried out. Absorbance was calculated from reflectance data by applying Kubelka-Munk transformation [Džimbeg-malčić et al., 2012]. Tauc plots $(\alpha.E)^2$ and $(\alpha.E)^{1/2}$ versus energy E are shown in Figure 7.3 (a) and 7.3(b), respectively. Figure 7.3(a) shows that only direct band transition is present near 3.59±0.02 eV while Figure 7.3 (b) shows that indirect band transition near 2.9 eV is present along with direct band transition for higher temperature annealed samples. Hexagonal $ZnTiO_3$ is also known to show indirect band transition while $Zn_2Ti_3O_8$ and Zn_2TiO_4 are reported to show direct band transitions [Conesa, 2013]. So, the onset of indirect band transition at 2.9 eV is attributed for hexagonal $ZnTiO_3$ and direct band transition at 3.59±0.02 eV is attributed to both Zn_2TiO_4 and $Zn_2Ti_3O_8$.

Vibrational spectra were collected using Fourier Transform Infrared (FTIR) spectroscopy system, as discussed in section 4.2.2.2. Figure 7.3(c) shows vibrational modes of metal and oxygen bonds for zinc titanate nano powder. These vibrational modes are similar to vibrational modes reported earlier in literature [Yamaguchi et al., 1987]. Vibration modes in 400-700 cm^{-1} are attributed to Ti-O stretching and modes below 400 cm^{-1} are attributed to the bending of Ti-O bond in TiO_6 octahedra. We observed similar vibrational spectrum for all calcinated zinc titanate samples and associated with presence of TiO_6 octahedral in these material systems. Vibration band at 426 cm^{-1} is present in lower calcinated temperature and it shows blue shift to 452 cm^{-1} for higher temperature calcinated temperature. All zinc titanate samples showed vibrational bands near 574 cm^{-1} and 724 cm^{-1}, consistent with earlier reported literature [Yamaguchi et al., 1987]. These vibrational modes are marked as ν (Ti – O) in FTIR spectrograph, Figure 7.3 (c) at respective wavenumbers, where symbol ν is representing the stretching of modes.

In this study, zinc titanate powder calcinated at lower temperature 750 °C having Zn_2TiO_4 and $Zn_2Ti_3O_8$ phases in nearly equal proportion is designated as sample A and zinc

titanate powder calcinated at temperature 900 °C is designated as sample B. These two zinc titanate samples are utilized for mesoporous electrode preparation and QDSSCs studies.

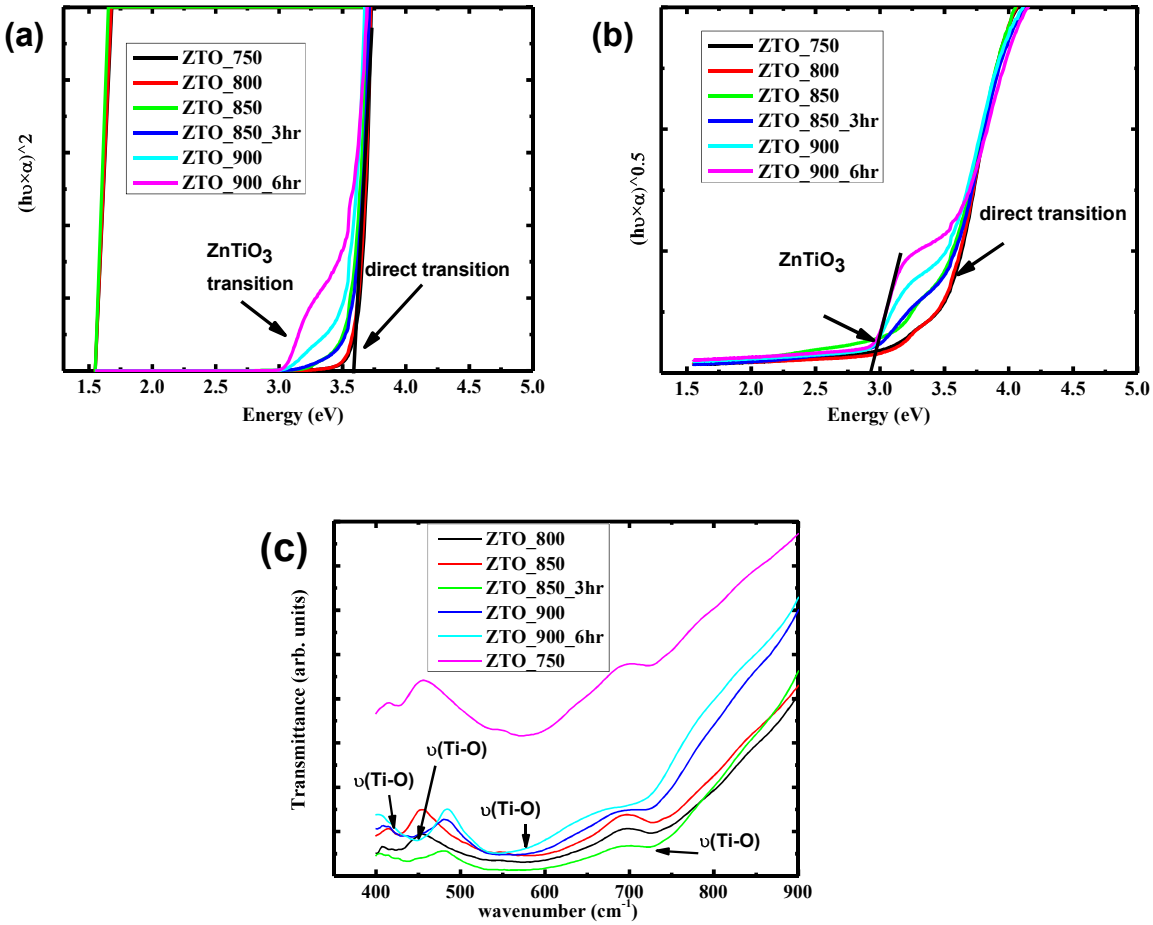

Figure: 7.3 (a, b) Tauc plot for zinc titanate powder with different calcination temperature and (c) vibrational spectra of zinc titanate nano powder with different calcination temperature indicated by labels.

7.3.3 Investigation of Microstructural Properties of Zinc Titanate Electrode

Surface morphology of zinc titanate (ZTO) electrode was investigated using scanning electron microscopy as discussed in section 4.2.1.2. Figures 7.4 (a) and 7.4 (c) show surface morphology of sample A while Figures 7.4 (b) and 7.4 (d) shows surface morphology of sample B. The low magnification images of electrode A and B, Figure 7.4 (a), and 7.4 (b), explain highly rough and porous surfaces. We can observe the agglomerated particles that can be attributed to the higher temperature calcination, leading to larger grain growth.

However, considerable differences are revealed from higher magnification images for electrode A and electrode B in Figure 7.4 (c) and 7.4 (d), respectively. Electrode A consists of smaller particulates of size < 100 nm while electrode B consists of larger particulates > 300 nm. Higher particulate size is attributed to the higher calcination temperature and associated grain growth, leading to larger grains for higher annealed samples.

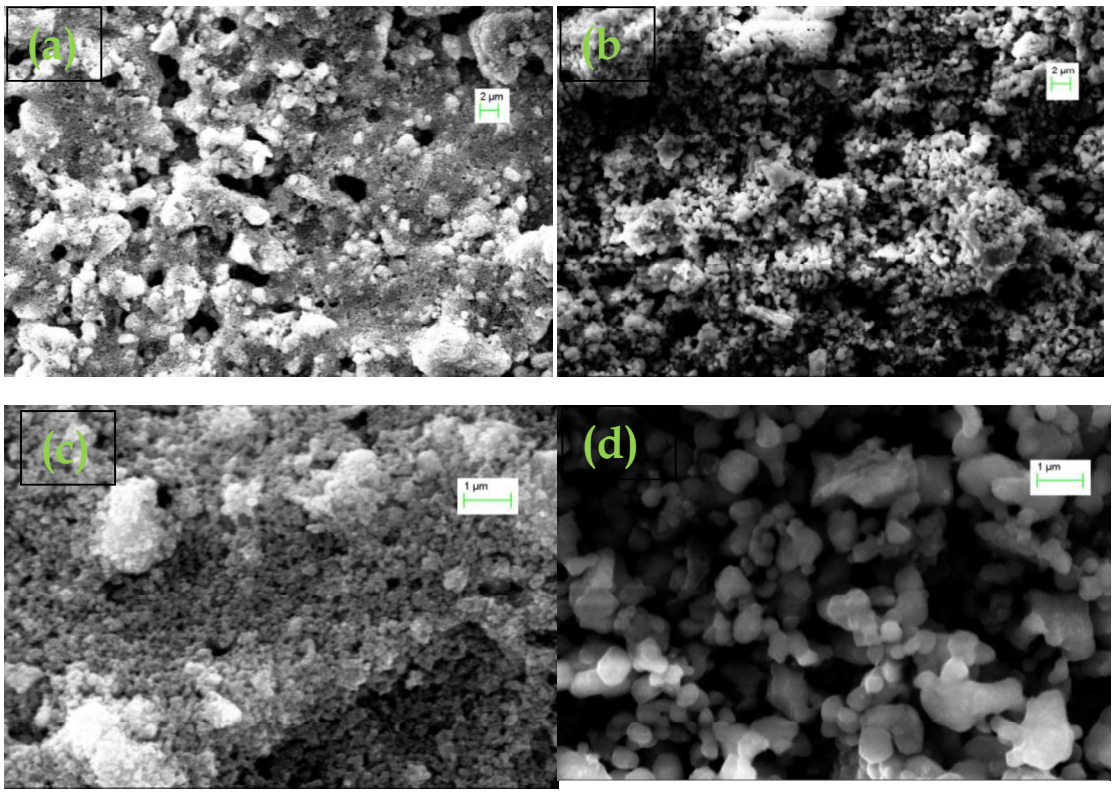

Figure: 7.4 Surface morphology of (a, c) electrode A for sample calcinated at lower temperature and (b, d) shows surface morphology of electrode B calcinated at higher temperature.

7.3.4 Investigation of Optical Properties of CdS Sensitized ZTO Electrode

Diffuse reflectance data is collected before CdS/ZnS sensitization of zinc titanate electrodes A and B and after CdS/ZnS sensitization of zinc titanate electrode A and B. Kubelka-Munk function [Džimbeg-malčić et al., 2012] is utilized to calculate absorbance from diffuse reflectance data.

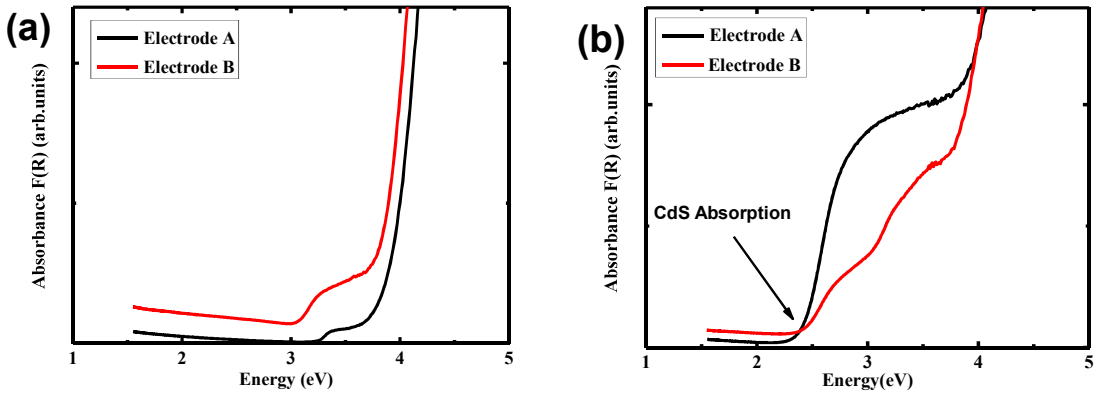

Figure: 7.5 (a) absorption of electrode A and B and (b) absorption of sensitized electrode A and B

Results are shown in Figures 7.5 (a) and 7.5(b), without CdS/ZnS sensitization showing absorbance of intrinsic zinc titanate electrode and with CdS/ZnS sensitization showing absorbance of CdS/ZnS along with intrinsic absorbance of zinc titanate respectively. A strong absorbance near 2.4 eV is attributed to absorbance from CdS quantum dots.

7.3.5 Investigation of Photovoltaic Properties of CdS/ZnS Sensitized ZTO Electrode

Cu_2S counter electrode along with polysulfide electrolyte is prepared as discussed in section 4.1.5.2 and 4.1.4, respectively. Cu_2S counter electrode and polysulfide electrolyte are utilized to prepare QDSSCs as discussed in section 4.1.6. These prepared QDSSCs are tested for their photovoltaic properties as discussed in section 4.2.3.1. The measured photovoltaic responses are shown in Figures 7.6 (a) and 7.6 (b) for sensitized electrodes A and B, respectively. A set of QDSSCs were tested (minimum 4 devices) and results are summarized in table 7.1 along with the best QDSSCs among investigated ones.

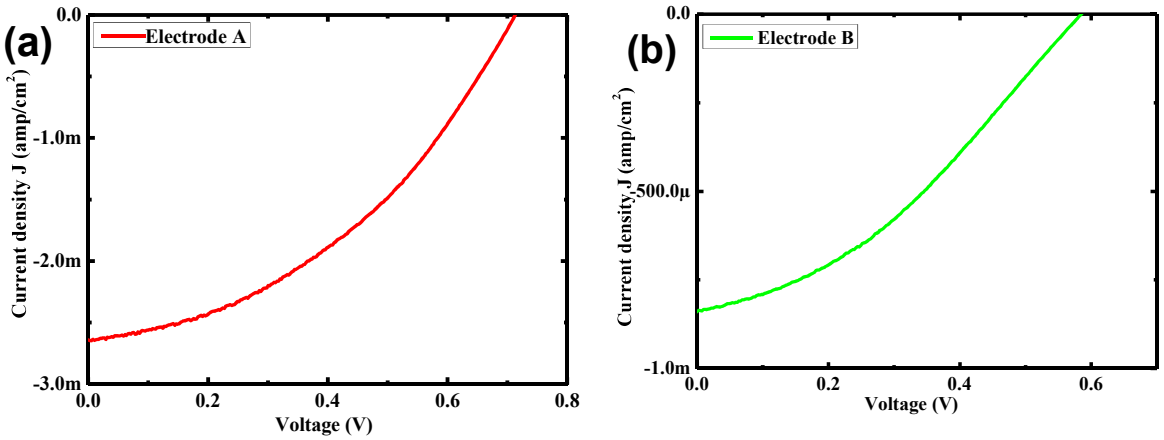

Figure: 7.6 Photovoltaic response of best device made of Zinc titanate (a) electrode A and (b) electrode B

We observed that photovoltaic response for electrode A is relatively superior to that of electrode B. The short circuit current densities are 2.2±0.3 mA/cm² and 0.76±0.10 mA/cm² for QDSSCs based on A and B electrodes, respectively. The open circuit voltage and fill factor are also higher for QDSSCS fabricated using electrode A, as listed in table 7.1.

Table: 7.1 Summary of photovoltaic performance of zinc titanate mesoporous electrode A and B based

QDSSCs based on different electrodes	J_{sc} (mA/cm^2)	V_{oc} (volt)	FF	Efficiency
Sample A (the best cell)	2.6	0.71	0.41	0.77
Sample A (average)	2.2+/-0.3	0.69+/-0.03	0.40+/-0.02	0.62+/-0.1
Sample B (the best Cell)	0.84	0.58	0.36	0.17
Sample B (average)	0.76+/-0.10	0.55+/-0.02	0.33+/-0.01	0.153+/-0.02

Impedance spectroscopy measurements are done on QDSSCs based on electrode A and B under dark in frequency range 100 KHz - 0.1 Hz. 10 mV ac signal is superimposed on open circuit voltage to record impedance data and respective Nyquist plots are shown in Figure 7.7. These results are fitted with equivalent circuit model suggest by Evan et al. as discussed in section 4.2.3.2. We found that recombination resistance of electrode B is four time higher than recombination resistance of electrode A as evident from diameter of arc in Nyquist plots. These results indicate that recombination processes affecting photovoltaic performance of electrode B are happening at lower time scales than the time scale of measurement (10^{-5} sec). That is the main reason we are observing lower photovoltaic response for electrode B. Bode plots for electrode A and B are plotted in Figures 7.7 (c) and 7.7 (d), respectively. Carrier lifetime for electrode A and B are calculated from these Bode plots and values are 13 ms and 17 ms for electrodes A and B, respectively [Kern et al., 2002]. Again higher carrier lifetime, observed for electrode B is in agreement with impedance measurements.

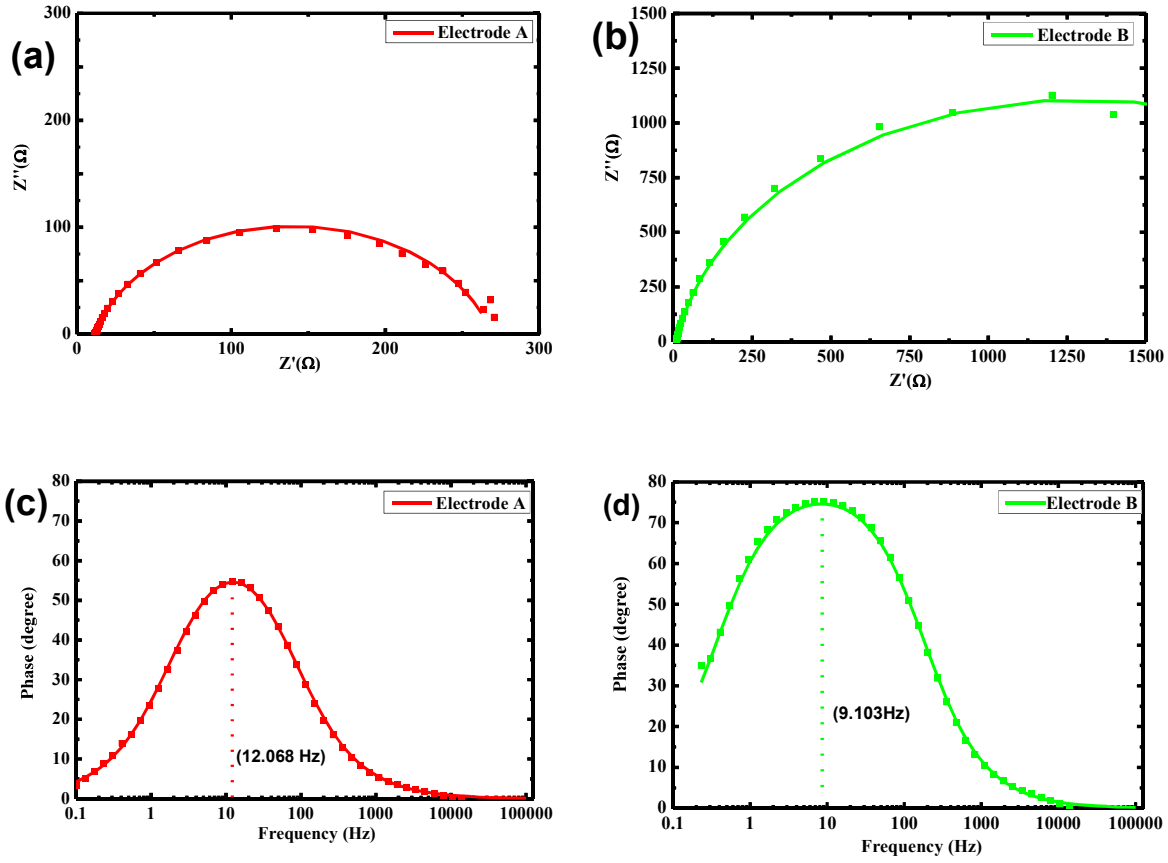

Figure: 7.7 (a) Nyquist plot for electrode A, (b) Nyquist plot for electrode B, (c) bode plot for electrode A and (d) bode plot for electrode B.

Variation in photovoltaic efficiency is plotted in Figure 7.8 (a) for QDSSCs investigated using electrodes A and B. The photovoltaic response for electrode A is always higher than that of electrode B. This superior photovoltaic performance for electrode A is attributed to (a)

different particulate size and (b) electronic properties which are relatively more suitable for efficient photovoltaic response.

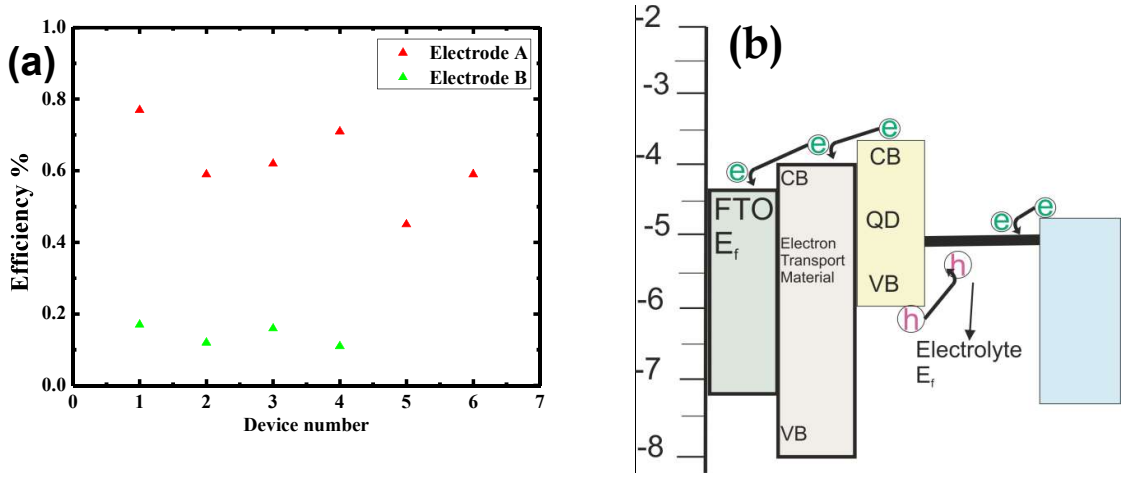

Figure: 7.8 (a) Distribution of photovoltaic performance of zinc titanate electrode and (b) schematic diagram of QDSSCs.

Electrode B is shown to have larger particulates following SEM investigation in section 7.3.3 and these larger particulates offer less surface area for QDs sensitization, an information that can be derived from normalized absorbance plot in Figure 7.5(b). Electrode B also consists of Zn_2TiO_4 and $ZnTiO_3$. These phases have direct band transition at 3.4 eV and indirect band transition at 2.9 eV respectively. So electrode B is made of phases those have higher difference in conduction level, hence additional recombination might be introduced at those levels. While electrode A consists of phases $Zn_2Ti_3O_8$ and Zn_2TiO_4, both of them have direct bandgap and similar bandgap transitions as evident from discussion in section 7.3.2. So these differences in electronic levels may be the deciding factors for final photovoltaic performance. Higher carrier lifetime observed in electrode B for injected electrons can be attributed to the higher particulate size that may have larger grain hence better diffusion length. Figure 7.8 (b) shows schematic diagram of desired energy levels in QDSSCs and it is evident from figure that lower the defect states in photoelectrode materials, and thus, lower probability for recombinations. The position of conduction band level is also important, and lower bandgap of hexagonal $ZnTiO_3$ might not be ideal from available photo-voltage, hence reducing photovoltaic performance.

7.4 Concluding Remarks

In this study, we have synthesized different crystallographic phases of zinc titanate using sol-gel method. Zn_2TiO_4 phase is present in all zinc titanate nano powder irrespective of calcination temperature while $Zn_2Ti_3O_8$ appears at lower calcination temperature and hexagonal $ZnTiO_3$ appears at higher calcination temperatures. At higher calcination temperature, $Zn_2Ti_3O_8$ starts converting in hexagonal $ZnTiO_3$. Photoelectrodes made of zinc titanate sample calcinated at lower temperature comprising of $Zn_2Ti_3O_8$ and Zn_2TiO_4 showed better photovoltaic response as compared to that of photoelectrodes made of zinc titanate sample calcinated at higher temperature comprising of $ZnTiO_3$ and Zn_2TiO_4. This study suggests that lower temperature calcinated zinc titanate may be a better photoelectrode material for QDSSC application.

...